Bulletin of the Seismological Society of America, Vol. 105, No. 5, pp. 2468–2479, October 2015, doi: 10.1785/0120140123

Systematic Changes of Earthquake Rupture with Depth: A Case Study from the 2010 M_w 8.8 Maule, Chile, Earthquake Aftershock Sequence

by Ali Tolga Şen, Simone Cesca, Dietrich Lange, Torsten Dahm, Frederik Tilmann,* and Sebastian Heimann

Abstract The very shallow part of subduction megathrusts occasionally hosts tsunami earthquakes, with unusually slow rupture propagation. The aftershock sequence of the 2010 M_w 8.8 Maule earthquake, offshore Chile, provides us with the opportunity to study systematic changes in source properties for smaller earthquakes within a single segment of a subduction zone. We invert amplitude spectra for double-couple moment tensors and centroid depths of 71 aftershocks of the Maule earthquake down to magnitudes M_w 4.0. In addition, we also derive average source durations. We find that shallower earthquakes tend to have longer normalized source durations on average, similar to the pattern observed previously for larger magnitude events. This depth dependence is observable for thrust and normal earthquakes. The normalized source durations of normal-faulting earthquakes are at the lower end of those for thrust earthquakes, probably because of the higher stress drops of intraplate earthquakes compared to interplate earthquakes. We suggest from the similarity of the depth dependence of normal and thrust events and between smaller and larger magnitude earthquakes that the depth-dependent variation of rigidity, rather than frictional conditional stability at the plate interface, is primarily responsible for the observed pattern. Tsunami earthquakes probably require both low rigidity and conditionally stable frictional conditions; the presence of long-duration moderate-magnitude events is therefore a helpful but not sufficient indicator for areas at risk of tsunami earthquakes.

Online Material: Table of earthquake inversion results for the 2010 M_w 8.8 Maule, Chile, aftershock sequence.

Introduction

Convergent plate boundaries, where oceanic plates subduct into the mantle along shallow dipping megathrust faults, are the regions where the largest earthquakes occur. The majority of such events show thrust-faulting characteristics on the interplate megathrust, and the depth of plate interface seismicity is mostly limited to less than 50 km (Bilek *et al.*, 2004). Because much of the subduction megathrust is usually offshore and thrust earthquakes cause vertical displacement at the surface, great subduction earthquakes often cause large tsunamis and are then referred to as tsunamigenic. For most earthquakes, seismologically determined slip models provide a reasonable prediction of tsunami heights. The seismic moment provides a reasonable guide to expected tsunami heights, when the location and approximate focal mechanism are known. For rare earthquakes, the relationship between seismic moment and tsunami size does not hold true, and the triggered tsunami is surprisingly large. Such earthquakes are known as tsunami earthquakes and are defined by their long rupture duration, low excitation of higher frequencies, and a tsunami disproportionately large for the given moment magnitude (Kanamori, 1972). Tsunami earthquakes have been documented in Japan (1896), Alaska (1946), the Kuril Islands (1963, 1975), Nicaragua (1992), Peru (1960, 1996), Java (1994, 2006), and Sumatra (1907, 2010).

Almost exclusively, tsunami earthquakes had their most significant rupture close to the trench. Therefore, most explanations invoke earthquake rupture along the very shallow part of the subduction interface and at least partially at the interface to unconsolidated sediments within the accretionary prism (e.g., Bilek *et al.*, 2004; Collings *et al.*, 2012; Lay *et al.*, 2012). Several effects in this environment contribute to the underestimation of the tsunami by seismological means. First of all, seismic observations are only able to infer the release of seismic moment M_0. This is then converted to an estimate of the displacement along the fault, d, according

*Also at Freie Universität Berlin, Berlin, Germany.

to where A is the area of a fault or fault patch with uniform slip, mostly assuming a standard value for the rigidity μ appropriate for continental crust. Because the rigidity in the accretionary wedge is presumably much lower (e.g., for the offshore central Chile refraction profile presented by Moscoso *et al.*, 2011), a given moment will translate into a much larger displacement along the fault, and thus a larger seafloor displacement and a larger tsunami. Furthermore, the coastal amplification effect is more pronounced if the seafloor displacement occurs in deep water, such as found above the lower forearc or accretionary wedge slope just landward of the trench, for example. The near-trench location of tsunami earthquakes thus exacerbates their severity. A final influence is exerted by the frictional properties of the plate interface. Because of the relatively low confining pressures and possibly the availability of free water from mineral dehydration reactions in the sediment package, the shallow part of the plate interface might be within a conditionally stable frictional regime, where ruptures cannot nucleate but can propagate if sufficiently perturbed (e.g., Scholz, 2002). Rupture within this regime might progress reluctantly, resulting in slow rupture propagation and thus the long rupture duration and deficiency in high frequencies characteristic of tsunami earthquakes. This results in reduced body-wave (M_b) and surface-wave magnitudes (M_s) compared to their moment magnitudes (M_w) (Ammon *et al.*, 2006). Furthermore, the deficiency in radiated high frequencies and the distance to the coast results in low perceived levels of shaking.

Modern seismological instruments and processing methods allow the recovery of the long-period part of the spectrum and are therefore able to avoid this limitation; however, in the context of tsunami early warning, there might be insufficient time available to properly record long-period phases such as the W phase (Duputel *et al.*, 2012).

If the conditions above are needed for tsunami events, then the smaller magnitude earthquakes within the same subduction segment might also have unusually long relative source durations, similar to those of their stronger neighbors that caused tsunamis. For simple ruptures, either unilateral or circular, the rupture duration τ is proportional to the fault dimension L divided by the rupture velocity v_r and $T \propto (L/v_r)$. The stress drop $\Delta\sigma$ is given by $\Delta\sigma \propto \mu(d/L)$. Combining these expressions with the moment equation given above results in a simple relationship between τ and moment,

$$M_0 = C\Delta\sigma v_r^3 \tau^3, \qquad (1)$$

in which C is a dimensionless constant near unity reflecting the detailed geometry of the rupture and details of the rupture propagation (e.g., unilateral versus circular). Dividing observed source durations by the cube root of M_0 (Houston *et al.*, 1998), one obtains normalized source durations (NSDs) for which the variation reflects variability in the stress drop and rupture velocity (Bilek and Lay, 1999). For circum-Pacific subduction zone thrust earthquakes, Bilek and Lay (1999) showed that depth and NSD are anticorrelated, such that shallow earthquakes (<15 km depth) have longer NSDs. Using subsets from different subduction zones, Bilek *et al.* (2004) added to the earlier database and observed strong regional differences. Events along the forearcs of Alaska, Mexico, and Peru show clear depth dependence of NSD, whereas events in Java and Japan show little or no depth dependence of the NSD.

The rupture velocity v_r itself is often thought to be a fixed fraction f (~0.8) of the shear-wave velocity V_S, that is, $v_r = fV_S$. In turn, V_S depends on the rigidity and density of the material surrounding the fault. Assuming the density is approximately fixed, Bilek and Lay (1999) argued that this pattern in source durations is primarily a result of the variation in rigidity. The alternative end member model of a variation in stress drop was also considered by Bilek and Lay (1999), but judged to be less important based on the independent evidence from structural studies for low shear velocities in the shallow parts of subduction zones.

In later articles, the same group still identified the rupture velocity as the controlling factor but now argued that the rupture process itself was different from deeper megathrust earthquakes for both tsunami earthquakes and the more moderately sized but still large earthquakes they studied, attributing this to the conditionally stable regime along the shallow plate interface, which was envisaged to be a patchwork of small, stronger, frictionally unstable asperities embedded in a conditionally stable or even frictionally stable (i.e., aseismic) background (Bilek and Lay, 2002). Although they did not state this explicitly, they now essentially argued that the long durations are partially or mostly attributable to a much lower ratio f than the usual 80%. Such exceptional slow rupture propagation is certainly highly plausible for some tsunami earthquakes, such as the 2010 Mentawai event (Newman *et al.*, 2011), for which the extreme rupture duration between 60 and 125 s for a length of ~50 km would require unrealistically low shear velocities of less than 1 km/s if f is assumed to be 80%. However, it is hard to apply this reasoning to events with $M_w <\sim 7$, because the rupture length is not known independently for them.

The longer NSD and conditionally stable frictional regime at shallow depths was suggested to be a combination of a variety of features and processes, such as fluid flow, thermal structure, and sediment deformation mechanisms (Bilek *et al.*, 2004). Because, in the conditionally stable regime, continued rupture requires a sufficiently large jolt to get started, one might expect that the propagation here can only be achieved by large earthquakes.

The previous studies mainly focused on moderate-to-strong plate interface earthquakes (e.g., with seismic moment above 10^{17} N·m, $M_w > 5.3$). In this study, we extend the magnitude range for the evaluation of the correlation among source parameters by including weaker events down to M_w 4, focusing on the subduction segment sampled by the aftershock series of the Maule 2010 earthquake, and making use of a dense deployment of over 130 broadband stations in this area to determine whether these events also follow the pattern identified by Bilek *et al.* (2004). Also, we do not limit

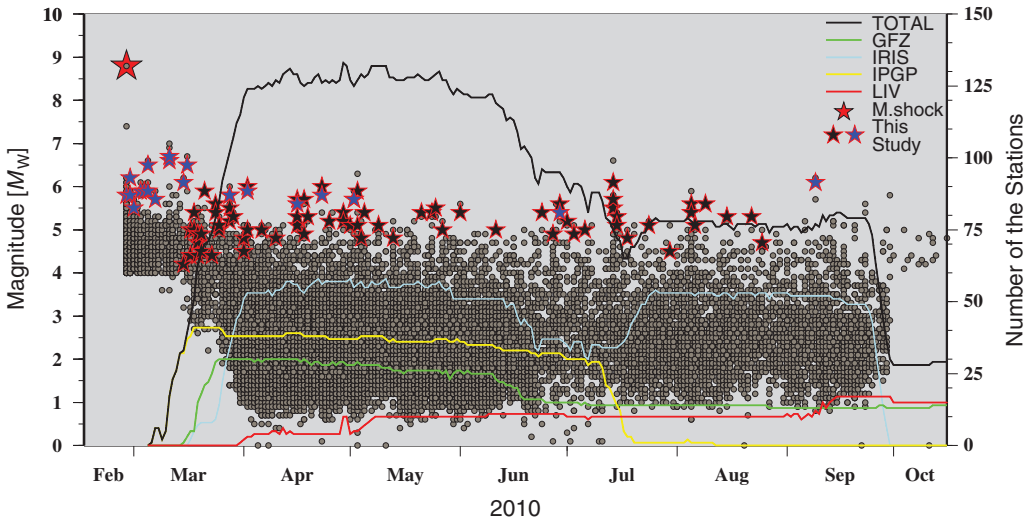

Figure 1. Temporal evolution of the aftershock sequence and International Maule Aftershock Deployment (IMAD) regional network coverage. Continuous lines represent the number of available stations installed by different institutions (see color scale) between March and October 2010. Gray dots represent 13,441 detected and located events, using at least 12 *P* phases from the local aftershock network (Lange *et al.*, 2012). The red, blue, and black stars denote the mainshock, aftershocks inverted with teleseismic data, and aftershocks inverted with local network, respectively.

our study to plate interface events, but examine all types of focal mechanisms.

The Maule 2010 Earthquake and Its Tectonic Setting

The 2010 Maule, Chile, earthquake is the sixth largest earthquake recorded instrumentally. The Global Centroid Moment Tensor (Global CMT) solution has a scalar moment of $M_0 = 1.8 \times 10^{22}$ N·m (M_w 8.8) for the mainshock and a centroid location of 35.95° S, 73.15° W, 23 km depth. The focal mechanism (strike 12°, dip 18°, and rake 112°) corresponds to a N12°E striking thrust fault, with low-angle-dipping plane consistent with the slab orientation. Coseismic slip inversions show a bilateral rupture propagation and a rupture length of ~550 km along the Chilean forearc. Two major slip patches north and south of the epicenter were resolved in coseismic slip inversions based on dense Global Positioning System observations and Interferometric Synthetic Aperture Radar data, where the peak slip was 16–20 m in the northern patch and around 10 m in the southern patch (e.g., Pollitz *et al.*, 2011; Moreno *et al.*, 2012). Although the Maule earthquake triggered a devastating tsunami, which is responsible for most of the fatalities of this earthquake (Fritz *et al.*, 2011), it is not a tsunami earthquake, as the magnitude of the tsunami was approximately as expected for an earthquake with M_w 8.8. Four main tectonic features shape the seismic characteristics of the upper plate along the Maule region, which are the north–south-trending thrust ridge (between 35° S and 37° S; Geersen *et al.*, 2011); possibly an outcrop of a seismically active splay fault at least in the northernmost part of the rupture (Lieser *et al.*, 2014); the Santa Maria fault (between ~36° S and 37° S; Melnick *et al.*, 2012); the Lanalhue fault (Glodny *et al.*, 2008), which is a major northwest–southeast-trending crustal fault system (between ~38° S and 39° S); and the extensional Pichilemu aftershock cluster (Farías *et al.*, 2010) in the overriding plate crust northeast of the northern slip patch of the Maule 2010 earthquake.

In response to the M_w 8.8 Maule earthquake on 27 February 2010, Chilean and international partners (Incorporated Research Institutions for Seismology [IRIS], the Centro Sismológico Nacional [CSN] at the University of Santiago, Institut de Physique du Globe de Paris [IPGP], GeoForschungsZentrum [GFZ], and University of Liverpool) installed a dense seismological network (International Maule Aftershock Deployment [IMAD]), which covered the whole length of the rupture zone between 32.5° S and 38.5° S (e.g., Beck *et al.*, 2014). Figure 1 shows the changing number of stations with time. This dense network is distributed over an area of about 600 km × 300 km, extending beyond the rupture area of the mainshock (Fig. 2). More than 160 seismic stations were deployed, 130 of them equipped with broadband sensors, and the remaining ones with short-period stations. The IMAD network was operational from mid-March 2010. Prior to this date, the earthquake location information used here is based on the Chilean catalog provided by the CSN and the National Earthquake Information Center (NEIC), which has a magnitude of completeness of 4.4 for South America (Legrand *et al.*, 2012).

The data from the IMAD network were used for several studies of aftershock seismicity (Fig. 2). Catalogs based on automatic picking and location algorithms were obtained by Lange *et al.* (2012; ~20,000 events in six months), Rietbrock *et al.* (2012; ~30,000 events in two months), and Hayes *et al.* (2013; 2375 events in nine months). All studies find that plate interface seismicity dominates the aftershock

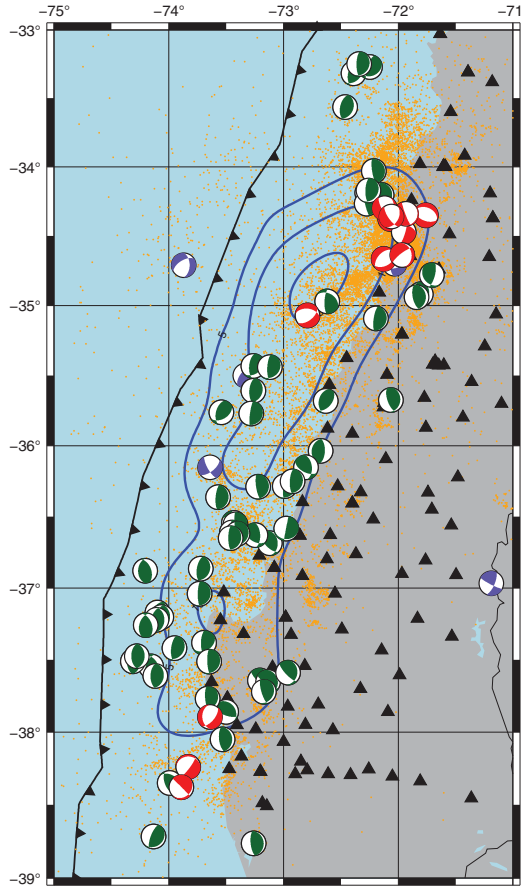

Figure 2. Distribution of events used in this study and the focal mechanisms resulting from waveform and amplitude spectra inversion (green, thrusts; red, normal; and blue, oblique or strike slip). Triangles denote IMAD broadband stations. Orange circles indicate aftershocks located with the IMAD network (locations from Lange *et al.*, 2012).

sequence and occurs mostly at depths between 25 and 50 km and distances to the trench between 50 and 160 km, with a pronounced gap at 35–40 km depth and at 120–150 km distance to the trench.

Two studies have carried out regional moment tensor (RMT) inversions for the IMAD dataset. Agurto *et al.* (2012) relocated 145 events from the Global CMT catalog in the period February 2010–March 2012 and then carried out a full-waveform RMT inversion with the software package ISOLated Asperities (ISOLA) (Sokos and Zahradnik, 2008), obtaining moment tensors (MTs) for 125 aftershocks. Using regional waveforms and following the approach of Herrmann *et al.* (2011), Hayes *et al.* (2013) determined MTs for 465 events.

In this study, we focus on source durations of the Maule 2010 aftershocks. We first derive MT solutions for a set of strong aftershocks of the Maule 2010 earthquake. We selected a subset of 56 events from the local catalog of Lange *et al.* (2012), with magnitudes $M_w > 4$, more than 12 P phases per event, root mean square less than 0.6 s, and hypocenter uncertainties less than 5 km. Focal mechanisms for the earlier largest aftershocks (limited to the magnitude range M_w 5.4–6.7) are obtained by the inversion of regional and teleseismic data downloaded from GEOFON and the IRIS Data Management Center, whereas events in the magnitude range M_w 4.2–5.6 following the deployment of IMAD have been studied using regional data only. We compare our solutions with published MTs and the slab geometry, and then further extend the inversion approach to obtain stable estimations of the source duration.

Methodology

Source inversion is performed using the Kiwi tools software (Cesca *et al.*, 2010, see Data and Resources; Heimann, 2011). The Kiwi tools were previously used to investigate a broad range of earthquake sources, including crustal and deep earthquakes and natural and induced seismicity at local, regional, and teleseismic distances (e.g., Cesca *et al.*, 2010; Buforn *et al.*, 2011; Şen *et al.*, 2013; Zhao *et al.*, 2014). Two different inversion procedures are adopted here, in consequence of the very different observation conditions throughout the aftershock sequence. The inversion MTs based on local network data can only be performed on data after 17 March 2010, when the aftershock network became operational (Fig. 1). Larger events are studied during the whole sequence using teleseismic data and sparse regional data from permanent stations.

For the regional inversion, targeting earthquakes with magnitudes M_w between 4.2 and 5.6 in the period 17 March 2010–25 August 2010, we adopt an automated multistep inversion scheme (Cesca *et al.*, 2010), which combines both amplitude spectra and full-waveform time-domain inversions in different steps. We used all available recordings from broadband stations located up to a maximum epicentral distance of 300 km. Traces were visually inspected to remove noisy data, and the control repeated upon the inversion to remove poorly fitting traces until a desirable fit was achieved. Synthetic seismograms and spectra are computed using the layered 1D velocity model from Haberland *et al.* (2009) and a reflectivity code (Wang, 1999). The inversion procedure is initiated with the source locations and origin times from the local catalog of Lange *et al.* (2012). The first inversion step is performed in the frequency domain, by fitting full-waveform amplitude spectra between 0.03 and 0.1 Hz to derive a pure double-couple (DC) point-source model. Because this inversion is not linear, the MT inversion is iteratively repeated for a number of starting MT configurations, following a Levenberg–Marquardt approach and minimizing the L2 norm misfit among the observed and synthetic amplitude spectra. As a result of this inversion step, we obtain the strike, dip, rake, centroid depth, and scalar moment. Uncertainties on point-source parameters are retrieved upon a bootstrap approach, by iterating the inversion and simulating different station configurations. The centroid depth uncertainty, which is relevant for the following discussion on the depth dependency of rupture processes, was always below 6 km. The advantage of the amplitude spectra inversion relies on its stability and lower dependence on precise trace alignment, which results

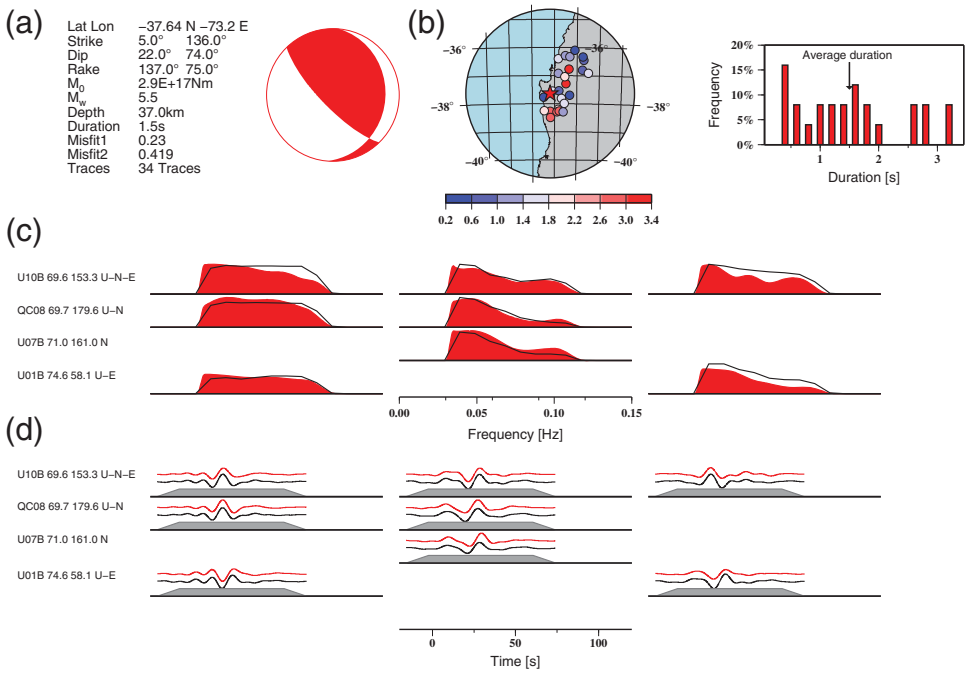

Figure 3. Source parameters, spectra, and waveform fit after regional moment tensor (RMT) inversion (for the 23 April 2010, 10:03:06 UTC, M_w 5.5 event. (a) Summary of double-couple (DC) source parameters derived by the RMT inversion. (b) Epicentral location (star) and apparent durations at different stations (circles; the color scale denotes apparent durations); the right plot illustrates the distribution of the apparent source durations, used to derive the mean event duration. (c) Comparison of normalized amplitude spectra between observed (red) and synthetic (black) data; the station information (epicentral distance in kilometers, azimuth, and components) is given on the left side. (d) Comparison of full waveforms in the time domain, showing observed (red) and synthetic (black) normalized full waveforms (gray areas denote the applied taper). Spectra and waveforms for only 4 out of the total of 20 stations used in the inversion are shown.

in a more stable inversion of the DC component of the MT at the cost of losing the phase information. To check for the presence of non-DC MT components, we also inverted for full MTs (for details, see Cesca *et al.*, 2013). In general, the full MT inversion reveals minor non-DC components (below 30%), most likely related to seismic noise, asymmetry of the network, and inaccuracy of the used 1D velocity model. Even for the remaining 17 events, for which larger non-DC components were obtained, the misfit improvement for the full MT solution, in comparison to the corresponding DC one, is not significant. The significance of the misfit improvement from a DC to a full MT source in view of the different number of free source parameters has been discussed in Cesca *et al.* (2013) through the adoption of different statistical information criteria. Upon these considerations, we consider our DC solutions to be more reliable and do not further discuss the full MT inversions.

Because of the intrinsic ambiguity of the amplitude information, the polarity of the fault cannot be resolved. However, the polarity is easily solved by comparing the synthetic waveforms for both polarities with observed displacements. Finally, we invert for rupture duration under a spatial point-source assumption. A set of apparent durations, one for each seismic station, is obtained by fixing the focal mechanism, depth, and moment, as retrieved from the previous inversion steps, and by carrying out a grid search for rupture duration. The adopted moment rate function is a half-period cosine function of variable duration. At each station, amplitude spectra are fitted according to an L2 norm for a broader frequency range, including higher frequencies up to 1.0 Hz, which are needed to resolve short-duration variations due to the finite-rupture process. We computed synthetic seismograms for durations up to 8 s; prior tests with finite-source synthetic data (Cesca *et al.*, 2011) demonstrated that full-waveform amplitude spectra below 1 Hz are still affected by changes in durations below 1 s; our approach is thus able to resolve durations of less than 1 s even when fitting frequencies up to only 1.0 Hz. First, we used this approach to estimate apparent durations at each station independently. Then the event rupture duration is obtained as the mean value of the apparent durations from all available stations. An example of an inversion, including point-source parameters, rupture duration, waveforms, and spectral fit, is shown in Figure 3. The rupture-duration grid search result is discussed further with the aid of Figure 4, which illustrates both the misfit curves for different single stations as well as for the whole dataset, when varying the rupture-duration parameter only. For most stations, the misfit curves show a clear minimum at the corresponding apparent durations. The difference among synthetic spectra and waveforms when varying the rupture duration is illustrated for a given station in Figure 4 (right) and highlights the significant improvement in

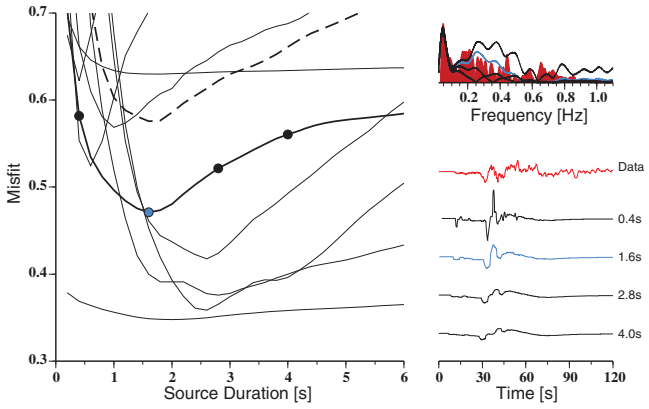

Figure 4. (Left) Misfit curves for different stations and the event shown in Figure 3 as a function of apparent source duration: the thick black lines denote the misfit curve for station U04B (for which spectra and waveforms are shown on the right), thin black lines are the misfit curves for all other stations, and a thick dashed line denotes the misfit curve when using all data. Circles indicate the misfits for the reference station for durations of 0.4, 1.6, 2.8, and 4.0 s. The best fit for the example station (blue circle) and, coincidentally, for the whole network is found for a rupture duration of 1.6 s. (Right) Comparison of amplitude spectra (top) and waveforms (bottom) at U04B, showing observed data (red line) and synthetics for different rupture durations (black lines for durations of 0.4, 2.8, and 4.0 s, and blue line for the best rupture duration of 1.6 s).

matching the observed waveform and spectra when an optimal rupture duration is chosen.

The lack of regional stations during the first days of the aftershock sequence forced us to use teleseismic data to analyze early events. Moreover, the largest aftershocks saturated most broadband recordings at regional distances and could only be studied with teleseismic data. For this reason, the inversion for MT solutions of the largest aftershocks (magnitudes M_w 5.4–6.8) in the period of 27 February 2010–23 October 2010 (Fig. 1, blue stars) was performed using regional and teleseismic data from permanent seismic broadband stations of different networks; waveform data and station metadata were accessed from the IRIS data center and converted to displacements. A station selection algorithm named "adaptive station weighting" is used for the teleseismic inversion (Heimann, 2011). The algorithm, which selects 60 stations (a value chosen to have a robust inversion within a reasonable time) within 100° maximal epicentral distance, aims to achieve a homogeneous distribution of seismic stations in terms of azimuths and epicentral distances. Additionally, it reweighs the data such that stations at all distances contribute approximately equally to prevent close stations, where absolute amplitudes are much larger, from dominating the inversion. However, rather than using a simple distance-dependent factor, the algorithm calculates synthetic seismograms for a number of representative sources and uses equivalent windows to the actual inversion to determine the weighting factor.

A different inversion scheme is used for the teleseismic data compared with the regional approach described above. It is still based on the Kiwi tools and combines frequency and time-domain inversion but is especially tuned for the analysis of larger events and the fitting of teleseismic records. The first inversion step derives DC point-source parameters by fitting amplitude spectra in the frequency domain. The resulting source-model configurations are then used in the following time-domain inversion, where DC source parameters, duration, centroid location, and centroid time are resolved. Given the inverted parameters and the adoption of an L1 norm, the inversion step is also nonlinear. In this second step, a gradient search method (Zhu *et al.*, 1997) is used to minimize the misfit between the observed and synthetics displacement traces in the time domain. The combined frequency–time-domain approach results in faster convergence with respect to a pure time-domain inversion. Both inversion steps optimize the fit of vertical *P* and transversal *S* phases. Data windows have a length of 60 s around each phase, and waveforms are band-pass filtered between 0.01 and 0.05 Hz. The inversion provides the following DC point-source model parameters: strike, dip, rake, depth, moment, centroid, and duration. For the duration inversion, a broader frequency range is used, including frequencies of up to 0.25 Hz. Uncertainties on all parameters are estimated using a bootstrap approach using random subsets of the 60 chosen stations (see also Heimann, 2011). For example, the uncertainties in duration are the result of the exploration of a 3D solution space, where duration, scalar moment, and depth are perturbed while the remaining source parameters are fixed (Fig. 5).

Results

We obtain 71 DC MTs and source durations for earthquakes with magnitudes between M_w 4.0 and 6.5 (Ⓔ see Table S1, available in the electronic supplement to this article). Many of the regional inversions (56 solutions, M_w 4.0–6.1) are characterized by asymmetric station distributions, with stations located on the Chilean mainland and epicenters located mostly offshore or near the coast (Fig. 2). Consequently, the azimuthal gaps for regional inversion using IMAD data vary between 58° and 302°. We obtain 21 solutions based on teleseismic data for earthquakes with M_w 5.4–6.5. The teleseismic estimate for one of the events originally considered (27 February 2010 23:02:02 UTC M_w 5.8) was found to have been biased by interference from an event with a similar magnitude in the Hindukush just ~20 minutes later, and this event was therefore excluded from further analysis. Six events could be analyzed using both regional and teleseismic inversion approaches. We find that regional and teleseismic inversion results are similar in terms of focal mechanisms, with differences never exceeding 15°, using the Kagan angle as a measure of focal mechanism similarity (Kagan, 1991) (Fig. 6), but nonnegligible changes among estimated durations, with differences up to a few seconds (the regional inversion durations are, on average, 57% shorter than the teleseismic inversion durations). Focal mechanisms are thus equally well resolved by the regional and teleseismic inversions. The duration inversion, however,

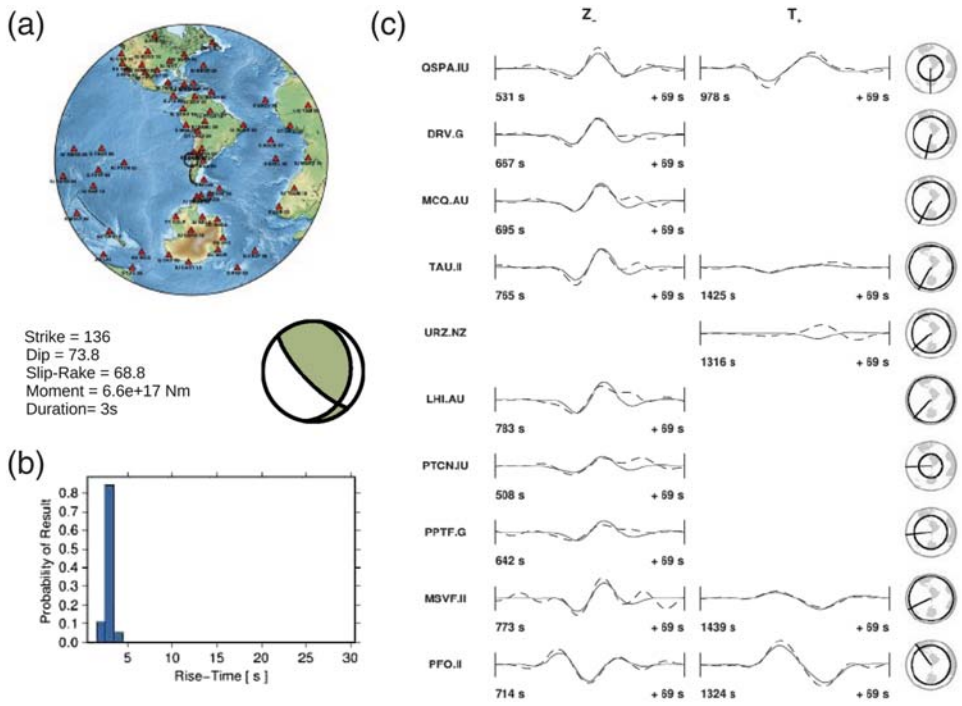

Figure 5. Source parameters and waveform fit after teleseismic moment tensor inversion (for the 23 April 2010 10:03:06 UTC, M_w 5.5 event, same as in Figs. 3 and 4). (a) Focal mechanism and distribution of the broadband stations used in this study (triangles). (b) Distribution of durations based on a bootstrap approach, used as an uncertainty measure. (c) Comparison of body-wave waveforms filtered with a 0.01–01 Hz band pass (dashed black lines are observed data, red lines are synthetics) for vertical *P* (left column) and transversal *S* (right column) waves for selected stations. The right panel shows epicentral distances and azimuths of those stations.

should be better resolved by the fitting procedure of the regional data, which considers higher frequencies. Therefore, we do not use any further the teleseismic inversion results for the six events for which both inversion setups were tested and, instead, only present the regional solutions in the Ⓔ electronic supplement and in Figures 2, 7, and 8. Also, we did not include the Maule mainshock or its largest aftershocks because, for events with M_w >∼7, it can no longer be assumed that the source can be represented by a spatial point source, as required by our inversion approach.

The centroid depths for the selected events vary between 5 and 65 km depth, with an average depth of 20 km. Most of the events (78%) have a thrust mechanism, whereas the remaining ones show normal or oblique normal focal mechanisms. Thrust mechanisms are distributed along the rupture area of the Maule 2010 mainshock. Most of the normal fault mechanisms occur in the continental crust of the overriding plate (source depths of less than 25 km) in the Pichilemu area, at about 34°–34.5° S. The observation of normal fault mechanisms in the forearc in the Pichilemu area was already described in dedicated publications by Farías *et al.* (2010) and Ryder *et al.* (2012). One normal-faulting event in our dataset occurred in the outer rise offshore the northern rupture patch, and there are also some normal-faulting events at the southern limit of the rupture zone, which appears to include events both in the upper and lower plates (with depths between 13 and 39 km).

Discussion

Comparison with Other Catalogs

We evaluate the consistency of our focal mechanisms with published DC solutions in the region of the Maule 2010 earthquake (Agurto *et al.*, 2012; Hayes *et al.*, 2013). For our dataset of 71 events, 43, 39, and 36 reference focal mechanism solutions are available in the catalogs of Agurto *et al.* (2012), Hayes *et al.* (2013), and Ekström *et al.* (2012) (Global CMT), respectively. In Figure 6, the difference between the catalogs is quantified using histograms of the Kagan angle (Kagan, 1991, 1992). For most events, we find an acceptable agreement, for example, with median values of the Kagan angles of about 20°, 28°, and 38°, when comparing to the results of Agurto *et al.* (2012), Hayes *et al.* (2013), and to the Global CMT catalog (Ekström *et al.*, 2012) (Fig. 6). Differences among estimated mechanisms can be explained by different data, velocity models, and inversion algorithms used by different authors. A more comprehensive agreement is found when comparing our solutions with the slab geometry (Fig. 6d). Here, the comparison is performed for the 63 thrust mechanisms, and the Kagan angle is computed with respect to hypothetical pure thrust mechanisms along planes oriented according to the slab gradient at the epicentral location based on the SLAB1.0 model (Hayes *et al.*, 2012, see Data and Resources). This result supports the quality of our solutions, as well as those in Hayes *et al.* (2013), because they both match well the geometry of the slab

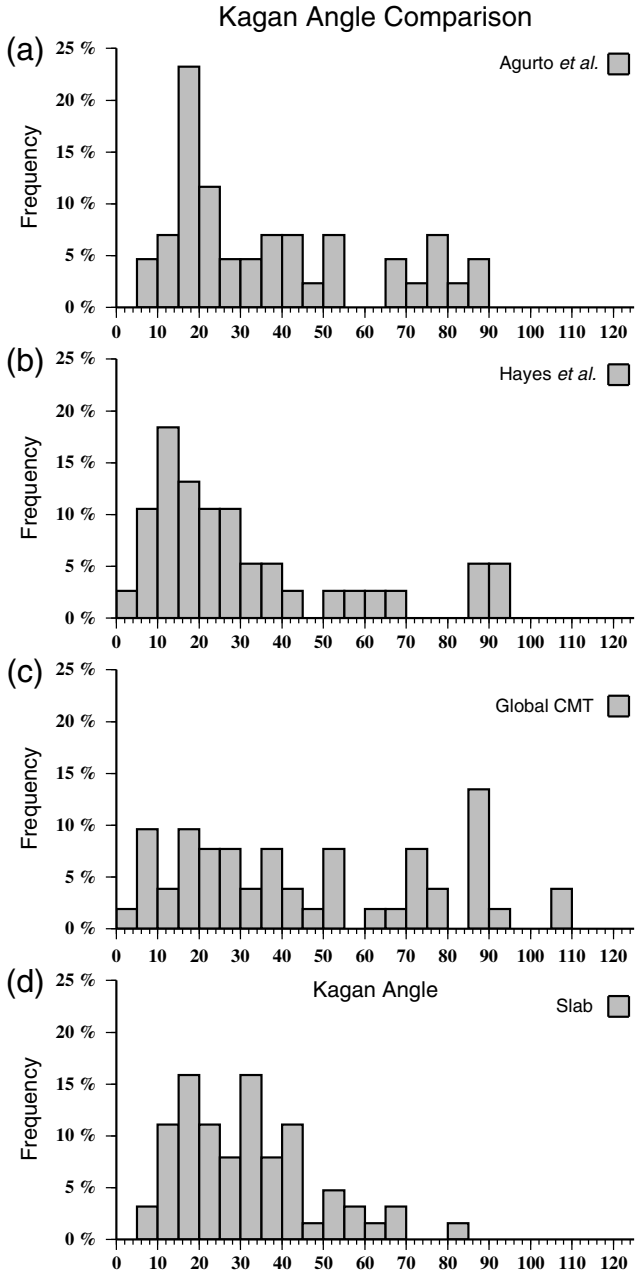

Figure 6. Comparison of DC inversion results with reference solutions and the slab geometry, using Kagan angle metrics. The comparison is performed against solutions by (a) Agurto *et al.* (2012), (b) Hayes *et al.* (2012), (c) Global Centroid Moment Tensor (CMT) catalog, and (d) pure thrust mechanisms oriented according to the 3D slab model by Hayes *et al.* (2012).

structure, although they were derived for 1D velocity models without any constraint based on the geometry of the slab structure. This result also suggests that most of the thrust earthquakes are indeed plate interface events.

Durations

To compare our findings with the larger events from a global study, we merged the results from Bilek *et al.* (2004) for Chile with the estimated parameters of our inversions (Fig. 7). Because the procedures for measuring durations employed by us are quite different from those of Bilek *et al.*, only the trends of both datasets should be compared, not absolute values. In Figure 7a, we plot the comparison between scalar moment and duration and evaluate it in a logarithmic scale plot. These results suggest a power law relationship between these two parameters, in agreement with previous results by Bilek *et al.* (2004) and theoretical expectations based on source scaling (see the Introduction and Kanamori and Anderson, 1975). Following Bilek *et al.*'s approach, NSDs are calculated by dividing the obtained absolute source duration by the cube root of moment, introducing a normalization constant appropriate for a reference magnitude (M_w 6 equivalent $M_0 = 1.16 \times 10^{18}$ N·m). The comparison of scalar moments and NSDs appears to show some increment of the NSD with the moment for the smaller events only. This means that larger events in this area have comparatively longer duration with respect to smaller ones and thus a higher stress drop or a lower rupture velocity. However, this relationship saturates around $M_0 = 10^{17}$ N·m and possibly reverses for very large magnitudes ($M_0 > 10^{18}$ N·m). Increasing stress drops with decreasing earthquake size were inferred for very small repeating earthquakes along the San Andreas fault (Nadeau and Johnson, 1998), and the corresponding scaling law is routinely assumed in the interpretation of repeating earthquakes in subduction zones (e.g., Igarashi *et al.*, 2003), but this relationship has not been verified independently. The expected lack of correlation between moment and depth is confirmed by the scattered distribution in Figure 7c.

We focus on the relationship between depth and NSD, which are clearly inversely correlated (Fig. 7d); shallow earthquakes tend to have longer durations, albeit with much scatter, confirming similar observations by Bilek and Lay (1999) and Bilek *et al.* (2004). In detail, shorter duration earthquakes (with NSD < 5 s) occur across the whole depth range of 10–50 km, whereas the maximum NSD drops significantly for increasing depth, with all events with NSD > 5 s shallower than 30 km and those with NSD > 10 s shallower than 20 km. Both regional and teleseismic inversions show this trend independently; and, in Figure 7d, the areas occupied by NSDs derived from both types of inversion overlap to a large extent, such that there is no reason to suspect any systematic bias between both modeling approaches. Our results thus successfully extend the previous finding by Bilek *et al.* (2004) to a much broader magnitude range by including moderate-magnitude earthquakes down to M_w 4. Compared to the durations estimated by Bilek *et al.* (2004) for Chilean earthquakes during the 1990s (plotted as stars in Fig. 7), our estimated NSDs show a similar trend but appear to be a little shorter on average. However, this difference probably does not relate to a physical effect, but just reflects the different methodology. The use of regional data allows the resolution of shorter durations, though, and this might also be reflected in the fact that the shortest NSDs (< 2 s) are all based on the regional inversions (Fig. 7d). The long NSDs for shallow events might indicate

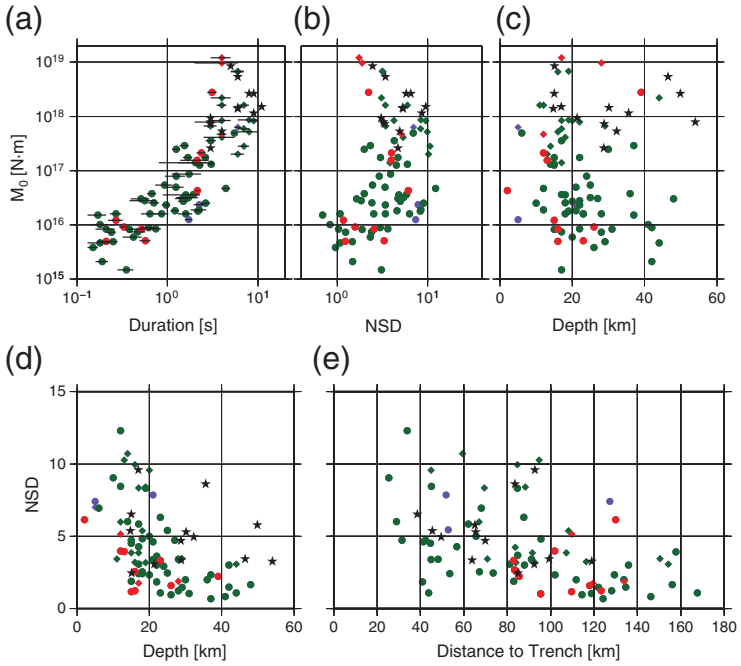

Figure 7. Comparison of (a) duration and scalar moment, (b) normalized source duration (NSD) and scalar moment, (c) depth and scalar moment, (d) depth and NSD, and (e) distance to trench and NSD. Colored circles denote our solutions, with fault mechanisms indicated by color (green, thrusts; red, normal; and blue, oblique, strike slip). Diamonds are those of the teleseismic inversions. Black stars are the results for earthquakes in Chile by Bilek *et al.* (2004); these apply to the whole Chilean margin, whereas the earthquakes in our dataset all have occurred within the Maule earthquake segment and are all aftershocks of this earthquake. In (a), the horizontal bars indicate the standard deviation for 1σ, which is equal to the 65% confidence level of the duration estimates.

either unusually low stress drops (large rupture area, small displacement) or low rupture velocity, or a combination of both. As Byerlee's law predicts lower absolute stresses for shallower faulting, it is not unreasonable to assume that stress drops have some depth dependency. Conversely, as explained in the Introduction, a depth-dependent rupture velocity can also reasonably be assumed. In the following, we will further explore these possibilities.

Normal-faulting events are strongly outnumbered by thrust earthquakes in our dataset but nevertheless cover a similar moment and depth range (Fig. 7c). However, the normal-faulting NSDs tend to be at the lower end of the range of NSDs for thrust earthquakes for a given depth (Fig. 7d), probably because of the long-standing observation that the stress drops of intraplate earthquakes are higher than those of interplate earthquakes (Kanamori and Anderson, 1975). Admittedly the real observable in most of these studies would also have been duration, with the stress drops being inferred based on the assumption of a constant rupture velocity, but larger stress drops for intraplate earthquakes compared to interplate ones are also observable for the largest earthquakes, where fault dimensions and slip can be determined independently (e.g., Ammon *et al.*, 2008). Notably, the NSDs of normal-faulting events show a very similar depth dependency to the overall dataset, that is, shallower events have, on average, longer NSDs. Broadly speaking, the slope of the quasilinear relationship between depth and maximum NSD is similar to that of thrust earthquakes, just that it applies at generally shorter durations.

Coming back to the possible interpretations of the long NSDs at shallow depths described in the Introduction, it appears implausible that the special conditions (fluid flow, entrained sediment, etc.) that were invoked to explain the presence of an extended conditionally stable frictional regime, and thus the unusually slow rupture on the megathrust, apply in all the regions affected by intraplate normal faulting. Yet these events show the same pronounced increase of NSD with decreasing depth. Furthermore, propagation of earthquake rupture into those parts of the fault area that are in the conditionally stable regime should only be possible for large earthquakes able to trigger instability within this regime. Nevertheless, our extended dataset, which includes events down to M_w 4.0, shows the same pattern of long NSDs for shallow earthquakes. This is still true even when just considering the subset of durations estimated from the regional inversions, which mostly consists of smaller events. Overall, this points to simple variation of rigidity with depth, as already proposed in Bilek and Lay (1999) as the main reason for the observed pattern, maybe making unnecessary the more complicated explanations advanced in Bilek and Lay (2002) and Bilek *et al.* (2004). On the other hand, in our dataset NSDs $> \sim 5$ s have only been measured for earthquakes with $M_0 > 10^{16}$ N·m ($M_w > 4.6$, Fig. 7b), and the required jump in shear-wave velocity, which should be proportional to $1/\text{NSD}$ (equation 1), by a factor of 3–4 from 50 to 15 km depth is too large to be realistic. Therefore, a systematic depth dependency of either stress drop or the ratio f, which governs

the ratio of rupture velocity to ambient shear-wave speed, must also contribute to the observed pattern. The apparent weak but systematic relationship between NSD and moment for smaller earthquakes could either result from a systematic stress-drop dependence on earthquake size as mentioned above—this is our preferred interpretation— or indeed an M_w of around 4.5 represents the critical earthquake size that still allows (slow) propagation into the conditionally stable regime. Of course, this critical magnitude will depend on many details, such as the degree and scale of heterogeneity of rate–state parameters along the fault surface. A further exploration of these questions is beyond the scope of this work and would require, on one hand, friction law-based earthquake cycle simulations to better understand earthquake propagation into stable and conditionally stable parts of the fault and, on the other hand, independent estimates of rupture sizes of moderate earthquakes from either high-resolution relocations of their aftershock series or the extension of finite-fault modeling or backprojection techniques to moderate-size earthquakes. The seismological approaches are technically challenging and require dense local networks or multiple small-scale arrays. Any explanation put forward must not only apply to the megathrust, but also apply equally well to intraplate earthquakes.

A surprising result is the variability of NSDs over nearly an order of magnitude at any given depth; this is true in particular for the shallower depths. This variability is unlikely to have arisen from uncertainties in the duration or depth estimates (< 6 km for depth, and typically less than 25% for duration), but instead most likely reflects a combination of heterogeneity of shear-wave velocity, different rupture styles (unilateral versus circular or bilateral), lateral or event-specific variability in stress drops or velocity ratio f, and the contrast between interplate and intraplate earthquakes. Some of the thrust earthquakes are likely to be intraplate earthquakes, for example, on splay faults as identified by Lieser *et al.* (2014), or in the downgoing plate, as proposed for some thrust earthquakes in the southern part of the rupture area by Hayes *et al.* (2013); without a detailed study these are hard to distinguish from plate interface events.

The spatial distribution of the long NSDs (Fig. 8) indicates that they are distributed along the strike of the rupture zone and not concentrated in any particular area. Of course, because most of the thrust earthquakes are located along the dipping slab, depth is strongly correlated with distance to the trench, and the plot of NSD versus distance to the trench (Fig. 7e) essentially reflects the NSD versus depth relationship. However, because the normal-faulting earthquakes are intraplate earthquakes, the distance to the trench is essentially uncorrelated to depth; and, accordingly, no obvious correlation between NSD and distance to the trench is identifiable for this type of earthquake, confirming that the variation of NSD is indeed real and related to earthquake depth and not, for example, an artifact of the back-azimuthal coverage, which for offshore events is naturally correlated with the distance to the trench in the regional inversions.

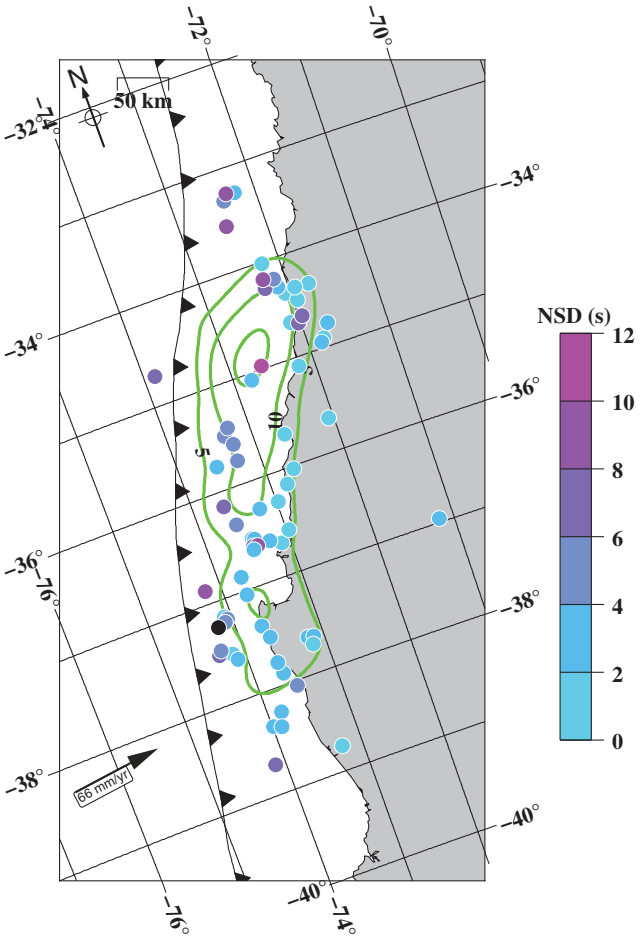

Figure 8. Durations and coseismic slip distribution (Moreno *et al.*, 2012), with 5 m contour lines.

Conclusion

We provide DC MT solutions and durations for 71 aftershocks of the 2010 Maule earthquakes, where we have combined regional and teleseismic data to cover the whole aftershock sequence in the magnitude range between M_w 4.0 and 6.8. Focal mechanism solutions indicate that the majority of these earthquakes occurred on thrust faults, with focal mechanisms similar to the mainshock; a few localized normal-faulting solutions are associated with crustal faults, the outer rise, and possibly the downgoing plate. The consistency of our solutions with those published in previous studies has been confirmed based on the analysis of focal mechanism similarities, using the Kagan angle (Kagan, 1991, 1992) as a metric. Following a similar approach, we find the fault planes of thrust focal mechanisms to align with the local orientation of a 3D model of the slab (Hayes *et al.*, 2012), suggesting a plate interface origin for most of them. The combined interpretation of focal mechanisms and source durations was used to verify that the negative correlation between NSD and depth, first proposed by Bilek and Lay (1999) for teleseismically recorded earthquakes, remains valid for weaker earthquakes down to M_w 4 and is observable along a single segment of the

subduction zone using the aftershock sequence of a single earthquake, the Maule 2010 event. Notably, although the normal-faulting earthquakes in our dataset tend to have shorter NSDs than the thrust earthquakes at the same depth, they follow a similar dependency of NSD on earthquake depth. We interpret these observation as an indication that depth-dependent variation of NSDs more likely results from variations of rigidity and stress drop than from special frictional conditions along the megathrust, but a definitive conclusion cannot be based on the NSD-versus-depth pattern alone and requires independent constraints on the slip and fault dimensions of moderate-sized earthquakes.

Whereas the inferred rigidity at shallow depth would certainly enhance the magnitude of any tsunami generated by an earthquake of a given moment, following essentially the reasoning in Bilek and Lay (1999), the usefulness of the NSDs of $M_w \sim 6$ earthquakes in identifying areas of the megathrust prone to tsunami earthquakes is less clear, given that NSDs of normal-faulting intraplate earthquakes have a similar depth dependency. This leaves open the question whether tsunami earthquakes are rare but, in principle, possible at all subduction zones or whether special conditions along the megathrust are needed and such areas at increased risk of tsunami earthquakes could potentially be identified in advance.

Data and Resources

The regional data from the International Maule Aftershock Deployment (IMAD) were provided by the Incorporated Research Institutions for Seismology Data Management Center and European Integrated Data Archive (International Federation of Digital Seismograph Networks codes 3A-2010-2012; XS 2010-2011; XY 2010; ZE 2010-2011; virtual network code IMAD). The Global Centroid Moment Tensor Project database was searched using www.globalcmt.org/CMTsearch.html (last accessed February 2014). The other earthquake catalogs were provided from Agurto *et al.* (2012) and Hayes *et al.* (2013). Source duration data from Bilek *et al.* (2004) used in Figure 7 are provided from Susan L. Bilek (personal comm., 2013). We used Kiwi tools for inversion of all earthquake data in this study between 2013 and 2014 (http://kinherd.org/; last accessed February 2014). We also used SLAB1.0 between 2013 and 2014 (http://earthquake.usgs.gov/data/slab/; last accessed February 2014) to examine the dipping of the subducting plate for the examined earthquake locations.

Acknowledgments

We thank Caltech, GeoForschungsZentrum (GFZ), Institut de Physique du Globe de Paris (IPGP), Incorporated Research Institutions for Seismology (IRIS), and the University of Liverpool for providing continuous waveform data for the International Maule Aftershock Deployment (IMAD) network. We thank the Servicio Sismológico Nacional de Chile (now renamed to Centro Sismológico Nacional) and the University of Santiago de Chile for logistical support during the deployment. We are grateful to Susan L. Bilek for providing us with her datasets. This work has been realized within the MARISCOS project, funded by German Research Foundation (DFG, Grant LA 2970/1-1). S. Cesca is funded by the MINE project (BMBF, German Ministry of Education and Research, Grant of project BMBF03G0737). We thank the IRIS and GEOFON data centers for hosting and distributing the data. Figures were generated using Generic Mapping Tool (Wessel and Smith, 1998). Two anonymous reviewers provided constructive criticism, which led to a significant improvement of this work.

References

Agurto, H., A. Rietbrock, I. Ryder, and M. Miller (2012). Seismic-afterslip characterization of the 2010 M_w 8.8 Maule, Chile, earthquake based on moment tensor inversion, *Geophys. Res. Lett.* **39,** L20303, doi: 10.1029/2012GL053434.

Ammon, C. J., H. Kanamori, and T. Lay (2008). A great earthquake doublet and seismic stress transfer cycle in the central Kuril islands, *Nature* **451,** 561–565, doi: 10.1038/nature06521.

Ammon, C. J., H. Kanamori, T. Lay, and A. A. Velasco (2006). The 17 July 2006 Java tsunami earthquake, *Geophys. Res. Lett.* **33,** L24308, doi: 10.1029/2006GL028005.

Beck, S., A. Rietbrock, F. Tilmann, S. Barrientos, A. Meltzer, O. Oncken, K. Bataille, S. Roecker, J.-P. Vilotte, and R. M. Russo (2014). Advancing subduction zone science after a big earthquake, *Eos Trans. AGU* **95,** 193–194.

Bilek, S. L., and T. Lay (1999). Rigidity variations with depth along interplate megathrust faults in subduction zones, *Nature* **400,** 443–446.

Bilek, S. L., and T. Lay (2002). Tsunami earthquakes possibly widespread manifestations of frictional conditional stability, *Geophys. Res. Lett.* **29,** no. 14, 1673, doi: 10.1029/2002GL015215.

Bilek, S. L., T. Lay, and L. J. Ruff (2004). Radiated seismic energy and earthquake source duration variations from teleseismic source time functions for shallow subduction zone thrust earthquakes, *J. Geophys. Res.* **109,** no. B09308, doi: 10.1029/2004JB003039.

Buforn, E., C. Pro, S. Cesca, A. Udías, and A. del Fresno (2011). The 2010 Granada (Spain) deep earthquake, *Bull. Seismol. Soc. Am.* **101,** no. 5, 2418–2430.

Cesca, S., S. Heimann, and T. Dahm (2011). Rapid directivity detection by azimuthal spectra inversion, *J. Seismol.* **15,** no. 1, 147–164, doi: 10.1007/s10950-010-9217-4.

Cesca, S., S. Heimann, K. Stammler, and T. Dahm (2010). Automated procedure for point and kinematic source inversion at regional distances, *J. Geophys. Res.* **115,** no. B06304, doi: 10.1029/2009JB006450.

Cesca, S., A. Rohr, and T. Dahm (2013). Discrimination of induced seismicity by full moment tensor inversion and decomposition, *J. Seismol.* **17,** no. 1, 147–163.

Collings, R., D. Lange, A. Rietbrock, F. Tilmann, D. Natawidjaja, B. Suwargadi, and J. Saul (2012). Structure and seismogenic properties of the Mentawai segment of the Sumatra subduction zone revealed by local earthquake traveltime tomography, *J. Geophys. Res.* **117,** no. B1, doi: 10.1029/2011JB008469.

Duputel, Z., L. Rivera, H. Kanamori, and G. Hayes (2012). *W*-phase fast source inversion for moderate to large earthquakes (1990–2010), *Geophys. J. Int.* **189,** no. 2, 1125–1147.

Ekström, G., M. Nettles, and A. M. Dziewoński (2012). The Global CMT project 2004–2010: Centroid-moment tensors for 13,017 earthquakes, *Phys. Earth. Planet. In.* **200,** 1–9.

Farías, M., G. Vargas, A. Tassara, S. Carretier, S. Baize, D. Melnick, and K. Bataille (2010). Land-level changes produced by the M_w 8.8 2010 Chilean earthquake, *Science* **329,** no. 5994, 916–916.

Fritz, H. M., C. M. Petroff, P. A. Catalan, R. Cienfuegos, P. Winckler, N. Kalligeris, R. Weiss, S. E. Barrientos, G. Meneses, C. Valderas-Bermejo, *et al.* (2011). Field survey of the 27 February 2010 Chile tsunami, *Pure Appl. Geophys.* **168,** 1989–2010, doi: 10.1007/s00024-011-0283-5

Geersen, J., J. H. Behrmann, D. Volker, S. Krastel, C. R. Ranero, J. Diaz-Naveas, and W. Weinrebe (2011). Active tectonics of the south Chilean marine forearc (35°S–40°S), *Tectonics* **30,** no. 3, doi: 10.1029/2010TC002777.

Glodny, J., K. Gräfe, H. Echtler, and M. Rosenau (2008). Mesozoic to Quaternary continental margin dynamics in south-central Chile

(36–42 S): The apatite and zircon fission track perspective, *Int. J. Earth Sci.* **97,** no. 6, 1271–1291.

Haberland, C., A. Rietbrock, D. Lange, K. Bataille, and T. Dahm (2009). Structure of the seismogenic zone of the southcentral Chilean margin revealed by local earthquake travel-time tomography, *J. Geophys. Res.* **114,** no. B01317, doi: 10.1029/2008JB005802.

Hayes, G. P., E. Bergman, K. L. Johnson, H. M. Benz, L. Brown, and A. S. Meltzer (2013). Seismotectonic framework of the 2010 February 27 M_w 8.8 Maule, Chile earthquake sequence, *Geophys. J. Int.* **195,** 1034–1051, doi: 10.1093/gji/ggt238.

Hayes, G. P., D. J. Wald, and R. L. Johnson (2012). Slab1.0: A three-dimensional model of global subduction zone geometries, *J. Geophys. Res.* **117,** no. B01302, doi: 10.1029/2011JB008524.

Heimann, S. (2011). A robust method to estimate kinematic earthquake source parameters, *Ph.D. Thesis*, University of Hamburg, Hamburg, Germany.

Herrmann, R. B., H. Benz, and C. J. Ammon (2011). Monitoring the earthquake source process in North America, *Bull. Seismol. Soc. Am.* **101,** 2609–2625.

Houston, H, H. M. Benz, and J. E. Vidale (1998). Time functions of deep earthquakes from broadband and short-period stacks, *J. Geophys. Res.* **103,** no. B12, 29,895–29,913.

Igarashi, T., T. Matsuzawa, and A. Hasegawa (2003). Repeating earthquakes and interplate aseismic slip in the northeastern Japan subduction zone, *J. Geophys. Res.***108,** 2249, doi: 10.1029/2002JB001920.

Kagan, Y. Y. (1991). 3-D rotation of double-couple earthquake sources, *Geophys. J. Int.* **106,** 709–716.

Kagan, Y. Y. (1992). Correlation of earthquake focal mechanisms, *Geophys. J. Int.* **110,** 305–320.

Kanamori, H. (1972). Tectonic implications of the 1944 Tonankai and the 1946 Nankaido earthquakes, *Phys. Earth Planet. In.* **5,** 129–139.

Kanamori, H., and D. L. Anderson (1975). Theoretical basis of some empirical relations in seismology, *Bull. Seismol. Soc. Am.* **65,** 1073–1095.

Lange, D., F. Tilmann, S. Barrientos, E. Contreras-Reyes, P. Methe, M. Moreno, B. Heit, H. Agurto, P. Bernard, J.-P. Vilotte, and S. Beck (2012). Aftershock seismicity of the 27 February 2010 M_w 8.8 Maule earthquake rupture zone, *Earth Planet. Sci. Lett.* **317/318,** 413–425, doi: 10.1016/j.epsl.2011.11.034

Lay, T., H. Kanamori, C. J. Ammon, K. D. Koper, A. R. Hutko, L. Ye, and T. M. Rushing (2012). Depth-varying rupture properties of subduction zone megathrust faults, *J. Geophys. Res.* **117,** no. B4, doi: 10.1029/2011JB009133.

Legrand, D., A. Tassara, and D. Morales (2012). Megathrust asperities and clusters of slab dehydration identified by spatiotemporal characterization of seismicity below the Andean margin, *Geophys. J. Int.* **191,** no. 3, 923–931.

Lieser, K., I. Grevemeyer, D. Lange, E. Flueh, F. Tilmann, and E. Contreras-Reyes (2014). Splay fault activity revealed by aftershocks of the 2010 M_w 8.8 Maule earthquake, central Chile, *Geology* **42,** 823–826, doi: 10.1130/G35848.1.

Melnick, D., M. Moreno, M. Motagh, M. Cisternas, and R. L. Wesson (2012). Splay fault slip during the M_w 8.8 2010 Maule Chile earthquake, *Geology* **40,** no. 3, 251–254.

Moreno, M., D. Melnick, M. Rosenau, J. Baez, J. Klotz, O. Oncken, A. Tassara, J. Chen, K. Bataille, M. Bevis, *et al.* (2012). Toward understanding tectonic control on the M_w 8.8 2010 Maule Chile earthquake, *Earth Planet. Sci. Lett.* **321/322,** 152–165, doi: 10.1016/j.epsl.2012.01.006.

Moscoso, E., I. Grevemeyer, E. Contreras-Reyes, E. R. Flueh, Y. Dzierma, W. Rabbel, and M. Thorwart (2011). Revealing the deep structure and rupture plane of the 2010 Maule, Chile earthquake (M_w 8.8) using wide angle seismic data, *Earth Planet. Sci. Lett.* **307,** 147–155, doi: 10.1016/j.epsl.2011.04.025

Nadeau, R. M., and L. R. Johnson (1998). Seismological studies at Parkfield VI: Moment release rates and estimates of source parameters for small repeating earthquakes, *Bull. Seismol. Soc. Am.* **88,** 790–814.

Newman, A., G. Hayes, Y. Wei, and J. Convers (2011). The 25 October Mentawai tsunami earthquake, from real-time discriminants, finite-fault rupture, and tsunami excitation, *Geophys. Res. Lett.* **38,** L05302, doi: 10.1029/2010GL046498.

Pollitz, F. F., B. Brooks, X. Tong, M. Bevis, J. H. Foster, R. Bürgmann, R. Smalley Jr., C. Vigny, A. Socquet, J. C. Ruegg, *et al.* (2011). Co-seismic slip distribution of the February 27, 2010 M_w 8.8 Maule, Chile earthquake, *Geophys. Res. Lett.* **38,** L09309, doi: 10.1029/2011GL047065.

Rietbrock, A., I. Ryder, G. Hayes, C. Haberland, D. Comte, S. Roecker, and H. Lyon-Caen (2012). Aftershock seismicity of the 2010 Maule $M_w = 8.8$, Chile, earthquake: Correlation between co-seismic slip models and aftershock distribution, *Geophys. Res. Lett.* **39,** doi: 10.1029/2012GL051308.

Ryder, I., A. Rietbrock, K. Kelson, R. Bürgmann, M. Floyd, A. Socquet, C. Vigny, and D. Carrizo (2012). Large extensional aftershocks in the continental forearc triggered by the 2010 Maule earthquake, Chile, *Geophys. J. Int.*, doi: 10.1111/j.1365-246X.2011.05321.x

Scholz, C. H. (2002). *The Mechanics of Earthquakes and Faulting*, Cambridge University Press, Cambridge, United Kingdom.

Şen, A., S. Cesca, M. Bishoff, T. Meier, and T. Dahm (2013). Automated full moment tensor inversion of coal mining induced seismicity, *Geophys. J. Int.* **195,** no. 2, 1267–1281.

Sokos, E. N., and J. Zahradnik (2008). ISOLA a Fortran code and a Matlab GUI to perform multiple-point source inversion of seismic data, *Comput. Geosci.* **34,** 967–977.

Wang, R. (1999). A simple orthonormalization method for stable and efficient computation of Green's functions, *Bull. Seismol. Soc. Am.* **89,** 733–741.

Wessel, P., and W. H. F. Smith (1998). New, improved version of the Generic Mapping Tools released, *Eos Trans. AGU* **79,** 579.

Zhao, P., D. Kühn, V. Oye, and S. Cesca (2014). Evidence for tensile faulting deduced from full waveform moment tensor inversion during the stimulation of the Basel enhanced geothermal system, *Geothermics* **52,** doi: 10.1016/j.geothermics.2014.01.003.

Zhu, C., R. H. Byrd, P. Lu, and J. Nocedal (1997). Algorithm 778: L-BFGS-B: Fortran subroutines for large-scale bound-constrained optimization, *ACM Trans. Math. Software* **23,** no. 4, 550–560.

GFZ German Research Centre for Geosciences Potsdam
Helmholtzstraße 6/7
14467 Potsdam, Germany
tolga@gfz-potsdam.de
simone.cesca@gfz-potsdam.de
torsten.dahm@gfz-potsdam.de
sebastian.heimann@gfz-potsdam.de
(A.T.Ş., S.C., T.D., S.H.)

GEOMAR
Helmholtz-Zentrum fuer Ozeanforschung Kiel
Wischhofstraße 1-3
FE Marine Geodynami, Room 8C-213
D-24148 Kiel, Germany
dlange@geomar.de
(D.L.)

GFZ German Research Centre for Geosciences Potsdam
Telegrafenberg
Building A 3, Room 103
14473 Potsdam, Germany
frederik.tilmann@gfz-potsdam.de
(F.T.)

Manuscript received 6 May 2014;
Published Online 11 August 2015